Identifying the impact of climate and anthropic pressures on karst aquifers using wavelet analysis

Jean-Baptiste Charlier, Bernard Ladouche, Jean-Christophe Maréchal

Identifying the impact of climate and anthropic pressures on karst aquifers using wavelet analysis

Jean-Baptiste Charlier*, Bernard Ladouche and Jean-Christophe Maréchal

BRGM, 1039 rue de Pinville, F-34000 Montpellier, France.

* Corresponding author: E-mail: j.charlier@brgm.fr; Tel: +33 (0)4 67 15 79 77; Fax: +33 (0)4 9 67 64 58 51.

Abstract

This paper assesses the implications of climate and anthropic pressures on short to long-term changes in water resources in a Mediterranean karst using wavelet analysis. This approach was tested on 38-year (1974–2011) hydrogeological time series recorded at the Lez spring (South France), which is exploited for water supply. Firstly, we investigated inter-relationships in the frequency domain by cross-correlation across multiresolution levels. Our results showed that rainfall and spring discharge are highly correlated in the high frequency

domain which reflects the hydrogeological response during flood events of typical highly karstified systems. Pumping and groundwater level are correlated in a lower frequency domain, illustrating seasonal to multi-year relationships. Secondly, continuous wavelet transform was applied to characterize the temporal variability of the inter-relationships involved. On the contrary to examples of "non-managed" karst aquifers in the literature, our results showed that the 10-year rainfall component was attenuate in the discharge signal. We assume that the reason is that the storage variations are strongly affected by pumping. This interesting result shows that possible long-term impacts of rainfall variability due to climate change may be masked by a high pumping rate. We showed also that despite an increase of the pumping rate from the 1980s, the stress on the groundwater resource does not increase from year to year. The present pumping strategy does not affect the drawdown in the long term, avoiding an over-exploitation of the aquifer. Finally, this study highlights the effectiveness of wavelet analysis in characterizing the response variability of karst systems where the hydrogeological regime is modified by pumping.

Keywords

Karst; Wavelet transform; Multiresolution analysis; Hydrogeological processes; Climate and anthropic pressures; Signal processing

1 Introduction

Groundwater is a major global water supply resource and is currently affected by two main stressors: climate and anthropic pressures. This is essentially true for aquifers pumped for water supplies in Mediterranean areas due to increased abstraction to meet the needs of the growing population in regions where the aquifer is irregularly recharged from one year to the next. Evaluating the impacts of climate and anthropic pressure on water resources in such regions is a major challenge, as most large aquifers are located in carbonate rocks subject to karstification. The hydrogeological response of karst systems is highly non-linear due to spatial and dynamic heterogeneities linked to fact that the void structure leads to the formation of preferential drainage axes (for reviews see Bakalowicz, 2005; Goldscheider et al., 2007). Some of karst aquifers are an important water source for major cities, particularly in Mediterranean regions. In these cases, the aquifer may be referred to as “actively managed” if the pumping rate is higher than the low water stage discharge rate of the system under natural conditions in summer. Then, groundwater storage is highly mobilized before the rainy autumn period that contributes most of the annual recharge each year. In this paper, we investigate climatic and anthropic impacts on the groundwater resource in a Mediterranean karst system under active water management. We ask whether pumping modified the hydrogeological response.

Wavelet analysis has become a powerful technique to study geophysical processes or signals (Kumar and Foufoula-Georgiou, 1997; Torrence and Compo, 1998). Decomposing a time series into time-scale space, this method localizes power variations within a time series. It is ideal for analysing non-stationary signals and identifying short- to large-scale periodic phenomena. In the field of hydrology, Continuous Wavelet Transforms (CWT) have recently

been used to study the effect of climatic phenomena on the stream flow regime (Labat et al., 2005; Massei et al., 2007; Labat, 2010; Fu et al., 2012), or to study runoff processes (Lafrenière and Sharp, 2003; Schaefli et al., 2007). CWT has been widely used to study the hydrogeological behaviour of karst systems. Comparing three springs, Labat et al. (2000; 2002) demonstrated the potential of wavelet analysis in identifying karst properties in relation to the degree of karstification. Structural heterogeneity also determines similar filtering properties on a small basin scale (Chinarro et al., 2011) and on a large scale (Hao et al., 2012): i) short time-scale signals are generally less filtered showing the transmissive role of the conduit network, ii) and high-energy large timescale signals can penetrate through the aquifer, illustrating the buffered role of the storage zone. In a Mediterranean context, this allows us to visualize annual and multi-annual scale components in relation to North Atlantic Oscillation (Andreo et al., 2006). The hydrogeological response has also been studied from a physico-chemical time series: to investigate transport properties and turbidity dynamics (Massei et al., 2006), to highlight temperature-runoff relationships during snowmelt (Mathevet et al., 2004), or to study groundwater variations in relation to the geological context (Slimani et al., 2009). Surface-groundwater interactions were also studied using CWT to improve understanding of river flow components in karst environments (Salerno and Tartari, 2009). But, there is a lack of knowledge regarding the identification of the respective role of climatic and anthropic pressures on the resource of karst aquifers.

Generally, CWT provides a good representation of energy distribution in time-scale space in all these works, highlighting the non-stationary nature and multi-scale behaviour of karst systems. However, to overcome limitations arising from intrinsic redundancy of the CWT representation, Labat et al. (2000; 2001) applied an orthonormal wavelet representation,

87 conserving the signal information, as a complementary approach. This multiresolution
88 analysis (discrete wavelet transform DWT) can be used to decompose a signal into successive
89 resolution levels. It allows the energy distribution across levels to be characterized and the
90 slow and fast components in a spring discharge time series to be distinguished. This
91 complementary DWT technique allows easier and more efficient interpretation of the energy
92 distribution across decomposition scales, assisting the study of the time-frequency space of
93 time series. It can thus greatly improve hydrogeological understanding of karst systems, but is
94 rarely found in the literature. From these latest studies showing the significant potential of
95 combined CWT and DWT, we expect that both approaches will be adapted to characterize on
96 groundwater resources the response to the cumulative effect of climatic and anthropic
97 pressures.

98 To assess the impacts of climatic and anthropic pressure on groundwater resources in a
99 karst system under active water management, this study aims to distinguish between the role
100 of rainfall and pumping on the karst response using wavelet analysis. As a first step, a
101 multiresolution analysis was performed in order to characterize the energy distribution across
102 scales. To identify the frequency domain where rainfall and pumping may influence the karst
103 system, we also present a cross-correlation across multi-resolution levels. As a second step,
104 continuous wavelet analysis was applied to track changes in phenomena over time, providing
105 information on the temporal variability of the karst response to climatic and anthropic
106 stressors. We applied these techniques on rainfall, pumping, discharge and piezometric time
107 series over a 38-year period (1974–2011) in the Lez aquifer in the South of France.

2 Site and measurements

2.1 Study site

2.1.1 Presentation

The Lez karst is located to the north of Montpellier in the Cévennes area in the South of France, in the western section of the Mediterranean zone. The Lez karst system is part of the North Monpelliérains karst hydrogeological unit bounded to the west by the Hérault River and to the north and east by the Vidourle River (Figure 1). The Lez karst aquifer is located in Upper Jurassic formations between 650 m and 800 m thick, located on both sides of the Matelles fault. The aquifer is unconfined to the west of the fault, while the section located to the east may be partially captive. In the zone lying under a Tertiary overburden, the aquifer is found in the Upper Jurassic and the Lower Cretaceous. A more detailed description of the study area can be found in Ladouche et al. (2014).

The Lez spring is the main outlet of the karst system (Figure 1). The spring outlet has been explored by cave-divers. They discovered a huge saturated sub-horizontal karst conduit developing more than 400 m inland (Figure 2), with a diameter ranging between 5 and 10 m. The exploration ended at 113 m deep below the spring outlet (-48 m ASL) in a zone where the conduit become wider. The hydrogeological basin is estimated to cover an area of 380 km² (Thiery et al., 1983). Different recharge zones can be distinguished, depending on the nature of the geological overburden. Recharge of the aquifer takes place predominantly in Jurassic limestone, occupying an area of 80 to 100 km² (Figure 1). Within the Cretaceous overburden (120 km²), losses occur locally along temporary watercourses and feed the aquifer locally during flood events. The Tertiary formations occupy an area of about 160 km². In general

these are considered as impermeable or almost impermeable and do not contribute to recharging the Lez karst aquifer.

The drinking water supply of the Montpellier agglomeration (with about 340 000 inhabitants) comes from the Lez karst spring since the 19th century (1854). Before 1968, this resource was used by gravity extraction, varying between 25.10^{-3} and 0.6 m^3/s (Paloc, 1979). From 1968 to today, the Lez karst spring is pumped according an active management strategy, the pumping flow rate during summer periods is greater than the spring's low-water discharge so as to mobilize the aquifer's stored reserves (Avias, 1995). From 1968 to 1982, water was abstracted by pumping in the Lez Spring basin (Figure 2a) at a rate of the order of 0.8 m^3/s. From 1983 onwards, deep boreholes located in the main karst conduit located upstream from the spring (Figure 2) have allowed pumping at a rate of up to 1.7 m^3/s (Avias, 1995). The pumping flow rates during low groundwater levels (1.2 to 1.7 m^3/s) currently exceed the pumping flow rates during high groundwater levels (0.9 m^3/s). The minimum groundwater level is fixed at 35 m a.s.l in the main conduit. The maximum drawdown permitted from pumping is thus 30 m below the overflow threshold of the spring (65 m a.s.l., Figure 2b). The lowest water level (i.e. 35 m a.s.l.) was reached during the 1995 hydrological cycle. For environmental reasons, a reserve flow rate of 0.160 m^3/s is restored for the Lez River downstream of the spring when it is not overflowing.

2.1.2 Hydrogeological background

The conceptual scheme of the Lez aquifer, built by Salado and Marjolet (1975) and completed recently by Bicalho et al. (2012), shows that the water from the Lez spring comprises a mixture of water from three main units in the aquifer: i) water from the aquifer in the Upper Jurassic limestone and the Lower Cretaceous; ii) surface water (losses) after

153 interacting with the Cretaceous formations; and iii) water from deep circulation in the
154 underlying Middle Jurassic, having long residence time.

155 The hydrogeological functioning of the Lez karst system has been characterized using
156 various rainfall-discharge modelling approaches accounting for pumping (Guilbot, 1975;
157 Thiery and Bérard, 1984; Fleury et al., 2009). These works showed that pumping during low
158 water periods draw out reserves coming from less transmissive zones in addition to the well-
159 drained reserves. An assessment of this pumping influence area around the network of karst
160 conduits give values of about 60 km² (Ladouche et al., 2014), representing only 15% of the
161 Lez spring's catchment.

162 Recent semi-distributed modelling approaches have given a first assessment of the
163 contributions of the main karst units. Simulating the groundwater level in the main drain at
164 the karst outlet using a semi-distributed lumped model, Ladouche et al. (2014) showed that
165 the eastern part of the Matelles fault is contributing 2-fold higher than the western part. This
166 result is coherent with previous works of Kong A Siou (2011) applying neuron models in a
167 semi-distributed approach.

168 *2.2 Hydrogeological data*

169 2.2.1 Measured data

170 Hydrogeological measurements have been carried out since 01 June 1974 to 31
171 December 2011. Figure 1 shows the locations of the monitoring sites from which data are
172 used in this study.

173 Daily precipitation intensity was measured in the three weather stations at St-Martin-de-
174 Londres, Valflaunes and Montpellier-Fréjorgues (Météo France, 2012).

Pumping discharge rates (*Qp*) in the karst conduit near the spring were recorded at daily intervals from 1974 to 2000, except during the 1991 to 1996 period when measurements were recorded at weekly intervals. Since 2000, *Qp* has been recorded at hourly intervals.

Until 1982, the piezometric level (*h*) was measured in the Lez spring basin at daily intervals. Since 1983, *h* has been measured directly in the main conduit in a borehole located upstream from the spring (Figure 2). Groundwater levels have been recorded on a daily basis from 1974 to 2000, except during the 1991-1996 period when measurements were recorded at weekly intervals. Since 2000, *h* has been recorded at hourly intervals. Since *h* expresses groundwater level relative to mean sea level, we also define a drawdown value *s* which expresses the groundwater level measured from the maximum head *hmax* ($s(t) = hmax - h(t)$). The value *s* was used instead of *h* in wavelet analysis in order to correlate an increased pumping rate with increased groundwater fluctuation (as the pumping rate increase is inversely correlated with the piezometric level).

Measured discharge at the Lez spring is denoted residual discharge (*Qr*), because the gauging station (Banque Hydro, 2010) is located 300 m downstream the outlet were pumping are carried out (Figure 2). *Qr* was measured between 1987 and 2007 at daily intervals. Data were corrected from the restored discharge (0.160 m^3/s) to the Lez River when the spring was dry. Before 1987, *Qr* was estimated from water level measurements in the basin. Minimum *Qr* value is zero.

2.2.2 Calculated data

Precipitation data (*P*) used in this study is the rainfall time series calculated by Ladouche et al. (2014) to optimize the contribution of three rain gauges in their developed transfer model used to simulate the spring discharge. The method - given by Pinault and

198 Allier (2007) - requires to compute the weighting factor of each rain gauge in order to
199 maximize the cross-correlation (see Section 3.1 for equations) between *P* and residual
200 discharge (*Qr)* measured between 1987 and 2007. The linear combination obtained for *P* is:

201 (Eq. 1) $P = 0.33P1 + 0.54P2 + 0.13P3$

202 where *P1* is the precipitation at St-Martin-de-Londres, *P2* is the precipitation at Valflaunes,
203 and *P3* is the precipitation at Montpellier-Fréjorgues (Figure 1).

204 During high water period - when overflows are observed at the spring (residual
205 discharge $Qr > 0$) - pumping is inferior to the natural discharge (*Qn*). *Qr* is interpreted as the
206 difference between *Qn* and *Qp*: $Qr = Qn - Qp$. According to Ladouche et al. (2014), pumping
207 mobilizes water stored only in the large conduit (where pumps are localised) during this
208 period, because no drawdown related to pumping was observed on piezometric *h(t)* time
209 series, as well as in the more distant connected piezometer Claret well (see Fig. 1 for
210 location). Consequently, during high water period, we assume that the storage flow mobilized
211 by pumping (*Qs*) is negligible (almost equal to 0).

212 During low water period - when pumping has dried the spring ($Qr = 0$) - pumping is
213 superior to *Qn*, and *Qp* is interpreted as the sum of *Qn* and the *Qs* (Ladouche et al., 2014): Qp
214 $= Qn + Qs$. Pumping thus mobilizes water reserves in the karst system that are inaccessible or
215 almost inaccessible in natural conditions. This phenomenon is reflected in a decrease of the
216 piezometric level in the karst conduit (groundwater level < 65 m a.s.l., Figure 2b).

217 The storage flow mobilized by pumping *Qs* is calculated by equation 2 (Ladouche et al.,
218 2014):

219 (Eq. 2) $$\begin{array}{l} if\ Qp \geq Qn\ then\ Qs = Qp - Qn\ \ and\ Qr = 0 \\ if\ Qp < Qn\ then\ Qs \approx 0\ \ and\ Qr = Qn - Qp \end{array}$$

This last equation requires to assess *Qn* which is unknown during low water level periods, as the Lez spring has been used since 1854 to supply drinking water (*Paloc*, 1979). During high water level periods (Figure 2a), *Qn* is higher than the pumping rate (*Qp*), and can be calculated as follows: $Qn = Qr + Qp$. During periods of low water levels (Figure 2b), *Qn* cannot be estimated from measurements. Recently, Ladouche et al (2014) have simulated the *Qn* time series using a transfer model combining a fast and a slow impulse response. Impulse responses were calculated by inverse modelling during high flow periods when $Qn = Qr + Qp$. The whole *Qn* time series was then simulated from 1974 to 2011 using the Tempo software (Pinault, 2001 ; Pinault et al., 2001a, b).

All hydrogeological time series for rainfall (*P*), Lez discharge (*Qr* and *Qn*), pumping discharge (*Qp*) and piezometric levels (*h*) for the period from 01 June 1974 to 31 December 2011 were synchronized at a time interval of 1 day.

2.2.3 Hydrogeological variables used to assess the karst response to stressors

This section presents the hydrogeological variables used as input and output to characterize the response of the karst system to climatic and anthropic stressors. Table 1 provides an overview of the set of variables, also showing the framework for interpreting their possible inter-relationships. The purpose of this guide is to help to interpret the results of the wavelet analysis used in this article.

The input variables representing specifically climatic pressure and anthropic pressures are precipitation *P* and pumping *Qp*, respectively. As the *Qs* variable is defined from *Qn* and *Qp*, (Eq. 2), and *Qn* is highly correlated to *P*, *Qs* integrates these both climatic and anthropic pressures. With regard to the output variables, the residual discharge *Qr* qualifies the karst

response to the rainfall during high flows periods. The water level (*h*) and especially the drawdown (*s*) qualify the karst stored changes due to inputs solicitation (precipitation and pumping).

Two ambiguous input-output relationships for the defined set of variables were identified. The *P*-*h* relationship is disrupted by the impact of pumping on the water level *h* (major drawdown during the summer). Similarly, *Qp* cannot be used to study properly the impact of pumping on *Qr*, since the latest is controlled by both *P* and *Qp* variables. Consequently, these two relationships were removed from the presented analysis. We will focus our analysis on the *P*-*Qr* relationship to assess the impact of the climate pressure on the karst functioning. The *Qp*-*s* relationship is used to assess the anthropic impact on the reserves. Finally, *Qs*-*Qr* and *Qs*-*s* relationships are used to assess the vulnerability of the resource to both climatic and anthropic pressures.

3 Wavelet analysis

The functions used are briefly presented on the basis of definitions put forward by several authors for wavelet analysis in geosciences (Kumar and Foufoula-Georgiou, 1997; Torrence and Compo, 1998; Labat et al., 2000; Bayazit and Aksoy, 2001; Grinsted et al., 2004; Jevrejeva et al., 2003; Maraun and Kurths, 2004). Wavelet transform can be used to decompose a time series over a time-scale space, thus providing a visualization of power distribution along time and frequency. It is suitable for analysis of non-stationary processes that contain multi-scale features, detection of singularities, or transient phenomena (see the review of Kumar and Foufoula-Georgiou, 1997). Thus, wavelet analysis gives a time-scale representation of the processes and of their relationships.

3.1 Continuous wavelet transforms

The wavelet transform can be seen as a bandpass filter of uniform shape and varying location and width (Torrence and Compo, 1998). The continuous wavelet transform (CWT) $W_x(\tau, a)$ of a time series $x(t)$ is given as follows:

(Eq. 3) $$W_x(\tau, a) = \int_{-\infty}^{+\infty} x(t)\Psi^*_{\tau,a}(t)\, dt$$

(Eq. 4) where $$\Psi_{\tau,a} = \frac{1}{\sqrt{a}}\Psi\left(\frac{t-\tau}{a}\right)$$

represents a group of wavelet functions, $\Psi_{\tau,a}$, based on a mother wavelet Ψ which can be scaled and translated, modifying the scale parameter a and the translation parameter τ respectively. $\Psi^*_{\tau,a}$ corresponds to the complex conjugate of $\Psi_{\tau,a}$. Wavelet functions have multi-scale properties, dilating or contracting a (a>1; a<1). When a increases, the wavelet covers a higher signal window. It allows the large-scale behaviour of x to be extracted. Conversely, when a decreases, the analysed signal window decreases, allowing local variations of x to be studied. Wavelet transform is thus characterized on the space scale by a window decreasing in width when we focus on local scale structures (high frequency), and widening when we focus on large scale structures (low frequency).

As in the Fourier analysis, a wavelet power spectrum (WPS) (also called a scalogram) $P_x(\tau,a)$ can be defined as the wavelet transform of $W_x(\tau, a)$:

(Eq. 5) $$P_x(\tau, a) = \left(W_x(\tau, a)\, W_x^*(\tau, a)\right) = |W_x(\tau, a)|^2$$

The choice of the appropriate analysis wavelet depends on the nature of the signal and on the type of information to be extracted from the time series (De Moortel et al., 2004). In this paper, we use the Morlet wavelet, as it is fairly well localized in both time and frequency space (Torrence and Compo, 1998). Other wavelet basis functions, such as Paul and Mexican

hat (DOG), were also tested in order to obtain better time localization, but gave the fairest results in both cases. Statistical significance level was estimated against a red noise model (Torrence and Compo, 1998, Grinsted et al., 2004). As CWTs are applied to time series of finite length, edge effects may appear on the scalogram, leading to the definition of a cone of influence (COI) as the region where such effects are relevant (Torrence and compo, 1998). The COI is marked as a shadow in the scalogram.

The covariance of two time series *x* and *y* is estimated using a cross wavelet spectrum (XWT) (also called a cross scalogram) $W_{xy}(\tau,a)$, which is the convolution of the scalogram of both signals:

(Eq. 6) $$W_{xy}(\tau,a) = \left(W_x(\tau,a)\, W_y^*(\tau,a)\right)$$

XWT reveals an area with a high common power value, but Maraun and Kurths (2004) reported that it appears unsuitable for significance testing of the interrelation between two series. These authors recommend the use of wavelet coherence (WTC) which is a measure of the intensity of covariance of the two series in the time-scale space. Beginning with the approach of Torrence and Webster (1999), the WTC of two time series *x* and *y* is defined as:

(Eq. 7) $$C_{xy}^2(\tau,a) = \frac{\left|S\left(a^{-1}W_{xy}(\tau,a)\right)\right|^2}{S(a^{-1}|W_x(\tau,a)|^2).S\left(a^{-1}\left|W_y(\tau,a)\right|^2\right)}$$

where *S* is a smoothing operator in both time and scale (see Torrence and Webster (1999) and Jevrejeva et al. (2003) for detailed mathematical expressions). The 5% significance level of WTC against red AR1 noise is estimated using Monte Carlo methods (Grinsted et al., 2004).

Neighbouring scales and times contain redundance information and are correlated (Maraun and Kurths, 2004), since the wavelet is translated continuously. However, some

approaches exist to limit this redundancy, as is the case with Discrete wavelet analysis (Labat et al., 2000; Bayazit and Aksoy, 2001) based on a wavelet with an orthogonal form.

3.2 Discrete wavelet transform and multiresolution analysis

In order to implement the wavelet transform on sampled signals, the discrete wavelet transform (DWT) can be used to discretize the scale and location parameters *j* and *k*, respectively. The discrete form of the wavelet transform of a time series *x(t)* is given according to Eq. 8:

(Eq. 8) $$W_x(\tau_0, a_0) = \sum_{-\infty}^{+\infty} x(t) \Psi^*_{\tau_0, a_0}(t)\, dt$$

(Eq. 9) where $\Psi_{\tau_0, a_0} = \frac{1}{\sqrt{a_0^j}} \Psi\left(\frac{t - k a_0^j \tau_0}{a_0^j}\right)$

with a_0^j being the scale parameter, τ_0 the translation parameter, *k* and *j* integers. $\Psi^*_{\tau_0, a_0}$ corresponds to the complex conjugate of Ψ_{τ_0, a_0}.

Multiresolution analysis (MRA) is able to study of signals represented at different resolutions. It can be used to decompose a signal into a progression of successive approximations and details in increasing order of resolution. Choosing particular values of a_0 and τ_0, in Eq. 8, namely $a_0 = 2$, and $\tau_0 = 1$, corresponds to the dyadic case used in MRA. The aim is to reduce/increase the resolution by a factor of 2 between two scales. Therefore, the approximation of a signal *x(t)* at a resolution *j*, denoted by A_x^j, and the detail of the same function at a resolution *j*, denoted by D_x^j, are defined by:

(Eq. 10) $$A_x^j(t) = \sum_{k=-\infty}^{+\infty} C_{j,k} \Psi_{j,k}(t)$$

(Eq. 11) $$D_x^j(t) = \sum_{k=-\infty}^{+\infty} D_{j,k} \Phi_{j,k}(t)$$

where $\Phi_{j,k}(t)$ is a scaled and translated basis function called the scaling function, which is determined with $\Psi_{j,k}(t)$ when a wavelet is selected. $C_{j,k}$ is the scaling coefficient given the discrete sampled values of $x(t)$ at resolution j and location k. It is calculated from $\Phi_{j,k}(t)$ in a similar way for the wavelet coefficient $D_{j,k}$ from $\Psi_{j,k}(t)$ (see Kumar and Foufoula-Georgiou (1997) for detailed mathematical expressions).

The signal $x(t)$ can be reconstructed from the approximation and detail components as:

(Eq. 12) $$x(t) = A_x^j(t) + \sum_{j=1}^{J} D_x^j(t)$$

where J is the highest resolution level considered. Since MRA ensures variance is well captured in a limited number of resolution levels, analysis of energy distribution in the sampling time series across scales give a good idea of the energy distribution across frequencies.

The choice of wavelet may influence the decomposition, particularly in low frequencies (Kumar and Foufoula-Georgiou, 1997). We accordingly tested various wavelet functions (Haar, Battle, Beylkin, Coiflet, Daubechies, Symmlet, Vaidyanathan) in order to assess the dispersion of results. Since the results were similar overall in the high frequency domain and less influenced in the lowest, we opted for the frequently used Daubechies 20 wavelet.

In order to quantify the relationship quality between two signals across scales, we used a multiresolution cross-analysis, combining multiresolution with cross-correlation (Labat et al., 2002). Cross-correlation can be used to determine the degree of similarity between two signals or two components (at the same resolution level for instance). The cross-correlation function (CCF) R_{xy} of two time series x and y, is calculated as follows:

(Eq. 13) $$R_{xy}(m) = \frac{C_{xy}(m)}{\sigma_x \sigma_y}$$

(Eq. 14) with $$C_{xy}(m) = \begin{cases} \frac{1}{n}\sum_{t=1}^{n-m}(x_t - \bar{x})\,(y_{t+m} - \bar{y}) & for\ m \geq 0 \\ \frac{1}{n}\sum_{t=1}^{n+m}(y_t - \bar{y})\,(x_{t+m} - \bar{x}) & for\ m < 0 \end{cases}$$

where C_{xy} is the cross-correlogram, m is the time lag, n is the length, and $\bar{x}$, and σ_x, and $\bar{y}$ and σ_y, are the average and the standard deviation of x and y, respectively.

More treatments of the wavelet transform (both continuous and discrete) and wavelet-based multiresolution (multi-scaling) analysis can be found in Chui (1992), Kumar and Foufoula-Georgiou (1997), and Mallat (2009) to which the reader is referred for more detail. Continuous wavelet analyses (CWT, XWT, and WTC) were carried out using a free Matlab software package (Mathworks, Natick, MA) kindly provided by Grinsted et al. (2004) at http://noc.ac.uk/using-science/crosswavelet-wavelet-coherence. The package includes code originally written by C. Torrence and G. Compo, available at: http://paos.colorado.edu/research/wavelets/, and by E. Breitenberger of the University of Alaska, adapted from the freeware SSA-MTM Toolkit: http://www.atmos.ucla.edu/tcd/ssa/. Multiresolution analysis was carried out using a free Matlab software package provided by the WaveLab Development Team and available at http://statweb.stanford.edu/~wavelab/.

4 Results

4.1 Variability of hydrogeological time series

This Section aims to describe the main variations over hydrological cycles from daily to annual data, in order to help readers to interpret the results of the wavelet analysis given in the next Sections 4.2 and 4.3.

4.1.1 Daily variability

Figure 3a shows daily hydrogeological time series of the Lez karst system over the last 38 years. Overall, the Mediterranean climate has a high rainfall intensity, for example attaining 177.5 mm/day in autumn 1976. The mean pumping discharge is around 1 to 1.1 m^3/s, exceeding the natural baseflow of the Lez spring. To better describe the variability of other hydrogeological data within a given year, Figure 3b zooms in on the 2002-2003 hydrological year. Heavy rainfall occurs in the end of the summer and in autumn with an intensity of up to 140 mm/day, generating the highest annual peak flow (15.4 m^3/s for *Qr*) at the Lez spring and a rise in groundwater level (*h*) from 65 to 69 m a.s.l.. In the winter and spring seasons, lower rainfall intensities generate lowest hydrodynamic response of the karst system as shown by small flood peaks inferior to 5 m^3/s and low groundwater variations. During this period of high groundwater level, *Qp* is near to 1.0 m^3/s and consistently below *Qn*: the spring is discharging (*Qr* > 0). At the beginning of the dry season in summer, *Qp* increases to 1.4 m^3/s and exceeds *Qn*. The spring consequently dries up (*Qr* is zero), and *h* starts to decrease (water is pumped directly from the conduit). During the low groundwater period in summer, the drawdown reaches 25 m (i.e. the piezometric level drops to 40 m a.s.l.). The saturated zone is highly mobilized by pumping and the reserve storage flow (*Qs*) increases to high values (around 1.0 m^3/s). The first abundant autumn rainfall in September 2003 led to rapid groundwater recovery to the initial level of 65 m a.s.l. as observed on the groundwater level time series (*h*). This phenomenon occurred in less than one day. The spring then starts to discharge again (*Qr* > 0) and another similar hydrological cycle begins.

4.1.2 Annual variability

To identify humid and dry periods and changes in the pumping discharge on an annual time scale, Figure 4 shows the annual hydrogeological time series expressed as deviation from the mean. The highest peaks for precipitation *P* occur in 1976-78, 1987-88, 1995-97, 2000-01, 2002-04 and 2008-09. Although annual discharge peaks (*Qr)* are clearly related to these humid years, there is no evidence of any relationship with groundwater level (*h).* Regarding annual pumping (*Qp*) and karst storage flow mobilized by pumping (*Qs*), we observed two periods. From 1974 to 1984 both time series are consistently below the mean (except in 1979-80 for pumping), unlike the period from 1984 to the present, during which the time series are higher for most of the time. These periods correspond respectively to a high and a low annual mean groundwater level, meaning that the groundwater level is primarily linked to pumping, leading to a rise in *Qs* as pumping rates increase. These results highlight the changes in water resource management from 1983, when water abstraction from deep boreholes began. This allows a higher pumping rate, less constrained in terms of drawdown. Before 1983, the position of the pump in the basin of the spring did not allow the water level to drop to more than 7 m, as opposed to 30 m today.

4.2 Multiresolution analysis

4.2.1 Energy distribution across scales

The main aim of this section is to visualize the distribution of energy across scales (or resolution levels) of the hydrogeological time series. Multiresolution was performed on daily data and the results for the first 10 multiresolution levels are shown in Figure 5. Overall, energy is distributed variably across levels in the hydrogeological time series. Regarding

input signals, precipitation *P* showed high energy mainly for levels 1 to 4 in the high frequency domain (corresponding to 1 to 8 days). This means that rainfall events on several days explain most of the variance in the overall *P* signal. The pumping discharge rate *Qp* showed high energy at all levels. Daily to weekly *Qp* variations are clearly highlighted as noise in the first levels. For levels 6 to 10, we observed a gradual decrease in energy during the 1980s. This was clearly visible on raw data (see Figure 3a). As with the pumping signal, the karst storage flow (*Qs*) showed high energy across levels. On the other hand, it shows a gradual energy increase in the 1980s. Regarding the output data for the karst system, the both residual discharge (*Qr*) and groundwater level (*h*) showed high energy distribution across scales, but different fluctuations over time. For *Qr*, energy distribution appears to be related to flood events for high frequencies (levels 1 to 4, corresponding to 1 to 8 days), and to seasonal and annual variations for lowest frequencies (levels 8, corresponding to 128 days). Energy variations for the groundwater level are in the same range regardless of the resolution level, meaning that scale has no apparent effect on groundwater variance. For all levels, *h* energy fluctuations over time in the 1980s are consistent with the previously observed gradual increase and decrease of *Qs* and *Qp* respectively.

In order to quantify the energy by multiresolution levels, the standard deviation (s.d.) was calculated by levels for each standardized time series (Figure 6). Overall, as previously described, *P* energy distribution across levels is totally different from other hydrogeological data. Figure 6 shows that s.d. of *P* decreases from 0.53 to about 0 for low to high multiresolution levels, meaning that the higher the frequency domain, the higher the energy. For other time series, we observe a similar main s.d. peak at level 8 (128 days), meaning that the highest energy is observed for medium levels, corresponding to intra-annual (seasonal)

periods. A second, lower s.d. peak is observed at levels 10 (512) and 12 (5.6 years) showing that high energy is also observed for annual and multi-year periodicities. Nevertheless, the s.d. of these time series is not negligible in the first levels, meaning that unlike precipitation, energy is still important across scales.

4.2.2 Multiresolution cross-correlation

To identify the frequency domain where input signals may influence karst system behaviour, in this section we present a cross-correlation function (CCF) across multiresolution levels (Figure 7). As shown in Table 1, the input signals used are *P*, *Qp*, and *Qs* and the output signals used are *Qr*, and *s* (instead of *h*). For each plot, two types of CCF were carried out. In a first case, as proposed by *Labat et al.* (2002), a CCF was carried out between two signals at the same multiresolution level *j* (black circles). In a second case, we chose to carry out a CCF between an overall input signal (i.e. a non-decomposed time series) and an isolated output signal at a given multiresolution level *j* (green stars). The maximum cross-correlation values R_{max} are shown in Figure 7 as a function of the multiresolution levels of the output signal expressed in days (at level *j*, the resolution corresponds to 2^{j-1} days).

In the first case (CCF between two signals at the same multiresolution level), the higher the multiresolution level, the higher the value of R_{max} up to 1. In contrast, we observed a R_{max} peak in the second case (CCF using an overall input signal). This difference shows that the output signal at a given multiresolution level is strongly influenced by the energy at lower resolution levels of the input signal. We can thus hypothesize that in the first case the CCF was controlled mainly by the resolution level of the decomposed times series. The R_{max} values of 1 (indicating that the output signal is exactly the same as the input signal) for the highest multiresolution levels are compatible with this hypothesis. Consequently, only the CCFs

between an overall input signal and an isolated output signal at a given multiresolution level (green stars) were considered for the analysis of multiresolution cross-correlation.

Regarding CCF between precipitation values as input and residual discharge values as output (*P-Qr* plots in Figure 7a), we observe a very similar evolution of R_{max} across scales. The highest correlation (around 0.30) occurs for levels 2 and 3, corresponding to 2 and 4-day resolution periods. This means that time series mainly co-vary in the high frequency domain on the flood event-time scale. A sill for levels 7 and 8 (64 and 128 days) is observed, leading the curve to decrease irregularly. This means that highest flood events imprint the discharge at the seasonal scale. For the highest multiresolution levels, both the rainfall and discharge time series become uncorrelated.

Regarding a CCF between pumping as input and drawdown as outputs (*Qp-s* plots in Figure 7b), we observe a bimodal distribution of *Rmax* across levels at level 8 (128 days) and level 13 (11.2 years) with R_{max} of 0.47 and 0.40, respectively. These results show that time series co-vary mainly for medium (intra-annual) and high (multi-year) levels, and that data are uncorrelated in the high frequency domain.

Regarding a CCF between storage flows as input and residual discharge and drawdown as outputs (*Qs-Qr* and *Qs-s* plots in Figure 7c and 7d, respectively), we observe a similar bimodal distribution of R_{max} across scales, compared to the CCF using *Qp* as input. At level 8, however, the highest correlations using *Qs* as input (0.39 and 0.61 for *Qs-Qr* and *Qs-s* respectively) showed that *Qs* is a better signal than *Qp* for characterizing the karst response to anthropic pressure within a given year. This is especially true for *s* as an output signal, because a strong correlation is also observed for the whole spectrum of energy as evidenced

by the R_{max} (0.84) of the CCF using an overall signal for input and output (dotted blue line in Figure 7d).

4.3 Continuous wavelet analysis

4.3.1 Wavelet power spectrum

Multiresolution cross-correlations provide information on frequency domains which are or are not correlated between two signals, but give no information on the temporal variability of their inter-relationships. The aim of this section is to investigate the short- to long-term influence of climatic and anthropic pressures on the karst response using Morlet continuous wavelet analysis (CWT). Because multiresolution analysis showed that pumping rate seems to not influence the hydrogeological response in very high frequencies (several days), CWT was carried out in the monthly to multi-annual frequency domain, in which anthropic impact may be investigated. Figure 8 presents scalograms for all hydrogeological variables to assess the spectral power variance of each hydrogeological signal at each level and at each time lag. On scalograms, the x- and y-axes represent the time-scale space, with frequencies expressed as periods in days (high frequencies or low periods at the top of the plot). The z-axis represents the value of the wavelet coefficient with low to high powers in blue to red colors.

Regarding the CWT for rainfall (*P* in Figure 8a), we identify structures in the high frequency domain (less than 128 days) which are not particularly less marked in the case of spring discharge (*Qr* in Figure 8d). This low signal attenuation in the 32 to 128-day band in *Qr* highlights a high transmissive function of the infiltration zone of the karst system. Generally, smallest semi-annual structures (128 to 256 days) appear concomitantly with the main annual ones during wet hydrological cycles in both *P* and *Qr* signals (i.e. in 1976-78,

1987-88, 1996-98, 2000-01, 2002-04 and 2008-09, see Figure 4). This shows the imprint of rainfall fluctuations on the karst system in autumn and in a lower manner in spring season. A scale-dependent structure for a 100 to 500-day period is observed in 1995 for *P*, highlighting the multi-scale distribution of energy among the highest rainfall events. A 10 to 8-year component is observed from 1991 to 2003 for *P*, reflecting a clear variation in large-scale rainfall distribution. This component is visible in the scalograms of *Qr*, but power is not above the 5% significance level except in the cone of influence (COI). Globally, on the contrary to high and medium frequencies, these results highlight an attenuation of the lowest frequencies in rainfall by the karst system. This is coherent with the multiresolution cross-correlation analysis presented above, showing a poor correlation between rainfall and discharge in the lowest frequencies.

Regarding CWTs for pumping, karst storage flow and groundwater level (*Qp*, *Qs*, and *h* in Figure 8b, 8c, and 8e, respectively), we identified a high variability of periodic structures over time before and after 1985. In the three scalograms, components are visible in the high frequency domain (below 128 days), for a seasonal period (128-256 days) and for an annual period. However, these structures, visible for *Qp* from 1974 to 1985, disappear from 1985 onwards, except for some small-scale and erratic annual structures. At the same time, all these structures appear for *Qs* and *h* in 1985 after a period without any visible component. This result is consistent with the multiresolution analysis showing a gradual decrease in *Qp* energy on all scales before 1985, and a concomitant gradual increase in *Qs* and *h* energies after this date. Again, the change in energy distribution observed since 1985 is related to the change in the water resource operating strategy since the creation of deep boreholes in 1983. On the

contrary to rainfall, no significant long-scale structures are visible in these three scalograms, despite high power in low frequencies of *Qp* and *s*.

4.3.2 Cross wavelet and coherence analysis

Inter-relationships between signals are investigated using cross wavelet transform (XWT) and wavelet coherence (WTC). Figure 9 presents cross-scalograms between rainfall, pumping and karst storage flow (as input signals) and spring discharge and groundwater level (as output signals) to help characterize the response of the system.

4.3.2.1 Response to climatic variations

Responses to climatic variations were investigated for XWT and WTC between precipitation as input and residual discharges as outputs (*P*-*Qr* plots in Figure 9a and 9b). Except for the driest years (notably 1990-1993) coinciding with low wavelet power, significant coherence between *P* and *Qr* appears throughout the time-scale space, suggesting strong relationships between both time series at all scales. XWT highlighted an irregular annual component during wet years when seasonal structures are also visible. Common features from the CWT stand out as being significant on the 8 to 10-year band from 1978 to 2005, showing a strong link between *P* and *Qr*.

4.3.2.2 Response to anthropic variations

Responses to anthropic pressure were investigated for XWT and WTC between pumping as input and drawdown as outputs (*Qp*-s plots in Figure 9c and 9d). The *Qp*-*s* scalogram showed an irregular annual component during mean and dry years when the surplus is not recharged, emphasizing the impact of pumping on the karst aquifer. Seasonal and high frequencies are also visible irrespective of the hydrological cycle (dry or wet)

showing that *Qp*-*s* relationships within a given year are not dependent on the annual recharge rate. No long-term influence is visible on the *Qp*-*s* scalogram.

4.3.2.3 Response to the cumulative effect of climatic and anthropic variations

Responses to the cumulative effect of climatic and anthropic variations were investigated for XWT and WTC between karst storage flow as input and residual discharges and drawdown as outputs (*Qs*-*Qr* plots in Figure 9e and 9f, and *Qs*-s plots in Figure 9g and 9h). For both the *Qs*-*Qr* and *Qs*-s cross-scalograms, two main components are clearly visible at 6 months and 1 year from 1985, showing a high level of co-variance between abstraction from groundwater storage and residual discharge and drawdown from the implantation year of the pumps directly in the karstic drain. For XWT *Qs*-*Qr*, the 6-month component appears more irregular since it is only visible when the karst system dries rapidly during the spring when the winter and spring recharge is insufficient to maintain a baseflow discharge above the pumping rate ($Qs > 0$ when $Qn < Qp$). For XWT *Qs*-s, we observed significant coherence throughout the time-scale space, showing strong relationships between both time series at all scales. Here, it is interesting to note that no significant common features in the wavelet power is visible in lowest frequencies, despite high coherence.

5 Discussion

The aim of this study was to identify using wavelet analysis the respective impacts of climatic and anthropic pressures on the water resource of a karst system under active water management. The first challenge was to identify the contributions of both stressors (namely rainfall and pumping rate, respectively) which concomitantly influence the hydrogeological

response. The second challenge was to track the evolution of phenomena over time and thus to identify the parameters leading to changes in the hydrogeological response of the system.

5.1 Frequency domains in which stressors influence the karst response

Multiresolution analysis (MRA) showed varying energy distribution across levels, meaning that the karst response was highly variable from high to low frequencies. Using multiresolution cross correlation, we determined the frequency domain where output signals (discharge and groundwater level) were most closely correlated to input signals (rainfall and pumping). Our results showed that rainfall and spring discharge are highly correlated in the high frequency domain which reflects the hydrogeological response during flood events of typical highly karstified systems. Pumping and storage flow are correlated to discharge and drawdown in the medium and low frequency domains, illustrating seasonal to multi-year relationships.

5.2 Climatic impact

Continuous wavelet transform (CWT) were used as a complementary approach of MRA to track tendencies and potential evolutions of the hydrogeological response. For rainfall and discharge CWTs, we showed that (i) high rainfall intensities are restored as in the discharge signal during flood events, (ii) an annual component is only visible during wet years in both signals (i.e. when extreme rain events occur), and (iii) the 10-year rainfall component was attenuate in the discharge signal. Despite this attenuation of the lowest frequencies observed in rainfall CWT, cross-wavelet transform (XWT) and coherence (WTC) were useful to provide evidence of long-term climate impacts on spring discharge. This 10-year component

590 should be related to rainfall oscillation in the 5 to 10-year band outlined by Pinault (2012) in
591 the western Mediterranean region. The attenuation of the large-scale rainfall component is
592 clearly different from examples of "non-managed" hydrosystems in the literature (Labat et al.,
593 2000; Chinarro et al., 2011; Hao et al., 2012), which showed that in general karst systems
594 filter less high frequencies (< 2 months) as in our study case, but imprint highly the lowest
595 frequencies due probably to inertial processes generated by the storage volume. Likely
596 explanations of the opposite process at large-scale observed in the Lez karst system is the
597 pumping strategy within a given year that regulates the storage variations (increasing or
598 decreasing the pumping rate according to the available water resource). This interesting result
599 shows that possible long-term impacts of rainfall variability due to climate change on the
600 karst system may be masked by the high pumping rate. However, we showed that XWT and
601 WTC may be a useful approach in order to detect it. The question thus arises of whether
602 pumping can modify the hydrogeological regime of the karst system.

603 ### *5.3 Anthropic impact*

604 Comparing multiresolution results and those of scalograms, a gradual increase in power
605 distribution was observed for the groundwater level in the 1980s and was concomitant with
606 the gradual increase and decrease in power observed for pumping *Qp* and storage flow *Qs*
607 respectively. This evolution is generated by the change in pumping strategy since the creation
608 of deep boreholes in 1983, when pumps were placed directly in the saturated zone of the
609 conduit. We assessed the frequency space of this evolution in terms of cross-scalograms and
610 coherence.

611 The impact of pumping on the hydrogeological response was characterized using *Qp-s*
612 XWTs. An irregular annual component was observed during mean and dry years on the

613 scalogram when there is no extra-recharge. Moreover, no large-scale component was
614 highlighted, meaning that any trend exists on the hydrogeological response to pumping. In
615 fact, regulations impose a maximum drawdown in the Lez aquifer (30 m below the spring),
616 limiting the impact of pumping on storage, even after the increase of pumping rate in 1983.

617 Cross wavelet analysis and coherence showed that *Qs* is a better signal than *Qp* to
618 explain the piezometric levels, with *Qs* reflecting both anthropic and climatic pressures as it
619 displays storage mobilization (i.e. pumping during periods of low groundwater levels). For
620 both *Qs*-*Qr* and *Qs*-s cross-scalograms, two main components are clearly visible at 6 months
621 and 1 year from 1983. Regarding the *Qs*-*s* cross-scalogram, the annual and 6-monthly
622 components appear continuous from 1983 to date, excluding irregularities in the 6-monthly
623 component during wet years. Multi-scale structures are also visible from 2 months to 1 year,
624 illustrating the scale-dependence of both series. This illustrates the anthropic and climatic
625 cumulative effects on the storage level, with continuous annual stress from the starting date of
626 active management. The absence of a large scale component between *Qs* and *s* (and between
627 *Qs* and *Qr*) can be explained by two phenomena: i) the high recharge rate during autumn in
628 Mediterranean areas, refilling the saturated zone each year, and ii) the pumping restriction
629 imposed by regulations stipulating the maximum drawdown. In this setting, the stress on the
630 groundwater resource does not increase from year to year and the present pumping strategy
631 does not affect the drawdown in the long term, avoiding an over-exploitation of the aquifer.

5.4 Implications on the understanding of the karst hydrogeological response

Multiresolution cross-analysis combined with cross wavelet analysis helps to improve our understanding of hydrogeological processes. Relationships between pumping *Qp* and groundwater level *s*, and between storage flow mobilized by pumping *Qs* and *s*, give informations on the storage evolution over time. Regarding multiresolution levels, we observed that *Qp* and *Qs* have a mainly mid- to long-term influence on the piezometric level in the conduit. In view of the continuous pumping strategy, we may assume that water stored in the fissured rock matrix is highly mobilized by pumping in the conduit during low water level periods. This is consistent with the results of Ladouche et al. (2014) which showed that the pumping induces mobilization of water in less transmissive units. In fact, conduit/matrix relationships generated by pumping have soon been observed during a 1-month pumping test in the Cent-Fonts karst system (Southern France) by Maréchal et al. (2008). The authors showed that both the fissured matrix (several kilometers away from the pumping well) and the conduit network were affected by the test. Indeed, pumping at the Lez aquifer outlet may influence the upstream part of the karst system over a long distance of about 20 km (Ladouche et al., 2014). The Matelles fault (location shown in Figure 1) is a major drainage axis and the direction of groundwater flow in the Lez aquifer has been ascertained by means of artificial tracer experiments (Marjolet and Salado 1975; Bérard 1983) and by interpretation of monitored water levels measured along this fault (especially at the Claret well - Figure 1) (Karam 1989; Conroux, 2007).

6 Conclusion

The aim of this study was to assess the respective impact of climatic and anthropic pressures on groundwater resources in a Mediterranean karst system under active water management. The main interest in our study was a combination of discrete (multiresolution) and continuous wavelet on 38-year hydrogeological time series recorded at the managed Lez karst aquifer (South France). Our main results showed that water management modifies the hydrogeological response at short and large-time scales. We assume that the reason why large-scale rainfall component do not appear in the spring discharge is that groundwater storage is highly affected by pumping. This result shows that possible long-term impacts of rainfall variability due to climate change may be masked by a high pumping rate. Despite an increase of the pumping rate from the 1980s, the stress on the groundwater resource does not increase from year to year. The current regulation of the hydrogeological conditions by controlling the drawdown – and thus the pumping rate - may be the reason why no long-term anthropic influence was identified. This indicates that the aquifer is currently not over-exploited. Thus, in case necessary, we expect that an increase of the pumping rate is again possible. This study highlights the effectiveness of wavelet analysis in characterizing the response variability of karst systems where the hydrogeological regime is modified by pumping. In order to establish water management scenarios under climatic changes, our approach may be useful to help decompose time series, extracting frequencies in which climatic and anthropic components are mainly localised, before their use in modelling approaches.

Acknowledgements

This work was conducted under the “Impact Karst” development project funded by BRGM. The authors wish to thank the *Montpellier Agglomération,* the Rhone-Mediterranean and Corsica Water Agency, the *Conseil Général de l’Hérault*, and the *Région Languedoc-Roussillon* for funding this work as part of the Lez-GMU project, and to thank Veolia for sharing time series data.

References

Andreo, B., P. Jiménez, J.J. Dura, F. Carrasco, I. Vadillo, and A. Mangin (2006), Climatic and hydrological variations during the last 117–166 years in the south of the Iberian Peninsula, from spectral and correlation analyses and continuous wavelet analyses. J. Hydrol. 324: 24–39.

Avias, J. (1995), Active management of Lez karstic spring, Herault, France, 1957–1994. Hydrogeologie, Editions du BRGM, pp. 113–128.

Bakalowicz, M. (2005), Karst groundwater: a challenge for new resources. Hydrogeol. J., 13, 148–160.

Banque Hydro (2010), http://www.hydro.eaufrance.fr; station No. Y3204020.

Bayazit, M, and H. Aksoy (2001). Using wavelets for data generation, Journal of Applied Statistics, 28(2), 157-166.

Bérard, P. (1983), Alimentation en eau de la ville de Montpellier. Captage de la source du Lez. Etude des relations entre la source et son réservoir aquifère. Rapport n°2 Definition des unités hydrogeologiques, BRGM Montpellier.

696 Bicalho, C.C., C. Batiot-Guilhe, J.L. Seidel, S. Van Exter, H. Jourde (2012),
697 Geochemical evidence of water source characterization and hydrodynamic responses in a
698 karst aquifer. J. Hydrol., 450–451: 206–218.
699 Chinarro, D., J. L. Villarroel, and J. A. Cuchi (2011), Wavelet analysis of Fuenmayor
700 karst spring, San Julian de Banzo, Huesca, Spain. Environ. Earth Sci., 65:2231–2243.
701 Chui, C.K. (1992), An Introduction on Wavelets, Academic Press, San Diego, 264 p.
702 Conroux, Y. (2007), Caractérisation du fonctionnement hydrodynamique de l'aquifère
703 karstique du Lez à l'état naturel. Mémoire Master 2, Univ. Avignon 2, 151 p.
704 De Moortel, I., S.A. Munday, and A. W. Hood (2004), Wavelet analysis: The effect of
705 varying basic wavelet parameters. Solar Physic., 222:203-228.
706 Fleury, P., B. Ladouche, Y. Conroux, H. Jourde, and N. Dörfliger (2009), Modelling the
707 hydrologic functions of a karst aquifer under active water management – The Lez spring. J.
708 Hydrol., 365(3-4):235-243.
709 Fu, C., A. L. James, and M. P. Wachowiak (2012), Analyzing the combined influence
710 of solar activity and El Niño on streamflow across southern Canada, Water Resour. Res., 48,
711 W05507.
712 Goldscheider, N., D. Drew, and S. Worthington (2007), Introduction. In: Goldscheider,
713 N., Drew, D. (Eds.), Methods in Karst Hydrogeology, Taylor & Francis, London. Int. Contrib.
714 Hydrogeol. 26, 1–8.
715 Grinsted, A., J. Moore, and S. Jevrejeva (2004), Application of the cross wavelet
716 transform and wavelet coherence to geophysical time series. Nonlinear Process. Geophys.,
717 11(5-6): 561–566.

718 Guilbot, A. (1975), Modélisation des écoulements d'un aquifère karstique (Liaison
719 pluie-débit). Application aux bassins de Saugras et du Lez. PhD thesis, Université des
720 Sciences et Techniques du Languedoc (Montpellier).
721 Hao, Y., G. Liu, H. Li, Z. Li, J. Zhao, and T.-C. J. Yeh (2012), Investigation of karstic
722 hydrological processes of Niangziguan Springs (North China) using wavelet analysis. Hydrol.
723 Process., 26, 3062–3069.
724 Jevrejeva, S., J. C. Moore, and A. Grinsted (2003), Influence of the Arctic Oscillation
725 and El Niño-Southern Oscillation (ENSO) on ice conditions in the Baltic Sea: The wavelet
726 approach, J. Geophys. Res., 108(D21), 4677, doi:10.1029/2003JD003417.
727 Karam, Y. (1989), Essai de modélisation des écoulements dans un aquifère karstique.
728 Exemple de la source du Lez (Hérault, France). PhD thesis, Université Montpellier II
729 Sciences et Techniques du Languedoc, 210 p.
730 Kong A Siou, L. (2011), Modélisation des crues de bassins karstiques par réseaux de
731 neurones. Cas du bassin du Lez (France). PhD thesis, Univ. Montpellier 2, 230p.
732 Kumar P, Foufoula-Georgiou E. 1997. Wavelet analysis for geophysical applications.
733 Reviews of Geophysics 35(4): 385–412.
734 Labat, D., R. Ababou, and A. Mangin (2000), Rainfall–runoff relations for karstic
735 springs. Part II: continuous wavelet and discrete orthogonal multiresolution analyses, J.
736 Hydrol., 238: 149–178.
737 Labat, D., R. Ababou, and A. Mangin (2001), Introduction of wavelet analyses to
738 rainfall–runoffs relationship for karstic basins: the case of Licq–Atherey karstic system
739 (France), Ground Water. 39(4): 605–615.

740 Labat, D., R. Ababou, and A. Mangin (2002), Analyse multirésolution croisée de pluies
741 et débits de sources karstiques. C. R. Geoscience 334: 551–556.
742 Labat, D., J. Ronchailb, and J. L. Guyot (2005), Recent advances in wavelet analyses:
743 Part 2 – Amazon, Parana, Orinoco and Congo discharges time scale variability. J. Hydrol.,
744 314: 289–311.
745 Labat, D. (2010), Cross wavelet analyses of annual continental freshwater discharge and
746 selected climate indices. J. Hydrol., 385: 269–278.
747 Ladouche, B, J.-C. Maréchal, and N. Dörfliger (2014). Semi-distributed lumped model
748 of a karst system under active management, J. Hydrol., 509, 215-230.
749 Lafrenière, M., and M. Sharp. (2003), Wavelet analysis of inter-annual variability in the
750 runoff regimes of glacial and nival stream catchments, Bow Lake, Alberta. Hydrol. Process.
751 17, 1093–1118.
752 Mallat, S. (2009), A wavelet tour of signal processing. The sparse Way. 3d Edition.
753 Academic Press, 805p. ISBN 13:978-0-12-374670-1
754
755 Maraun, D., and J. Kurths (2004), Cross wavelet analysis: significance testing and
756 pitfalls. Nonlinear Process. Geophys. 11, 505–514.
757 Marechal, J.C., Ladouche, B., Doerfliger, N., Lachassagne, P., 2008. Interpretation of
758 pumping tests in a mixed flow karst system. Water Resour. Res. 44, W05401,
759 doi:10.1029/2007WR006288
760 Marjolet, G. and J. Salado (1975), Contribution à l'étude de l'aquifère karstique de la
761 source du Lez (Hérault). III. Etude des écoulements d'eau dans les calcaires fissurés et

762 karstifiés du site du futur captage de la source du Lez. Université Montpellier II. Mémoires du
763 C.E.R.G.A, Tome IX-Fac. III. 139p.

764 Massei, N., J.P. Dupont, B.J. Mahler, B. Laignel, M. Fournier, D. Valdes, and S. Ogier
765 (2006), Investigating transport properties and turbidity dynamics of a karst aquifer using
766 correlation, spectral, and wavelet analyses. J. Hydrol., 329: 244– 257.

767 Massei, N., A. Durand, J. Deloffre, J. P. Dupont, D. Valdes, and B. Laignel (2007),
768 Investigating possible links between the North Atlantic Oscillation and rainfall variability in
769 northwestern France over the past 35 years, J. Geophys. Res., 112, D09121,
770 doi:10.1029/2005JD007000.

771 Mathevet, T., M. Lepiller, and A. Mangin (2004), Application of time series analyses to
772 the hydrological functioning of an Alpine karst system: the case of Bange-L'Eau-Morte.
773 Hydrology and Earth System Sciences. 8(6): 1051-1064.

774 Météo France (2012), Rainfall data, 1974–2011. METEO France, Toulouse, France

775 Paloc, H. (1979), Alimentation en eau de la Ville de Montpellier. Captage de la source
776 du Lez, commune de St-Clément (Hérault). Etude documentaire préalable à l'établissement
777 des périmètres de protection. Note de synthèse. Rapport BRGM 79 SGN 319 LRO, 47p.

778 Pinault, J.L., 2001. Manuel utilisateur de TEMPO, logiciel de traitement et de
779 modélisation des séries temporelles en hydrogéologie et en hydrogéochimie. BRGM, Report
780 RP-51459-FR, 221 p.

781 Pinault, J.-L, H. Pauwels, and C. Cann (2001a), Inverse modeling of the hydrological
782 and the hydrochemical behavior of hydrosystems; application to nitrate transport and
783 denitrification. Water Resour. Res. 37(8):2179-90.

784 Pinault, J.-L., V. Plagnes, L. Aquilina, and M. Bakalowicz (2001b), Inverse modeling of
785 the hydrological and the hydrochemical behavior of hydrosystems; characterization of karst
786 system functioning. Water Resour. Res. 37(8):2191-204.
787 Pinault, J.-L., and D. Allier (2007), Regionalization of rainfall for broad-scale
788 modeling: An inverse approach, Water Resour. Res., 43, W09422.
789 Pinault, J.-L. (2012), Global warming and rainfall oscillation in the 5–10 yr band in
790 Western Europe and Eastern North America. Climatic Change: 114:621–650. DOI
791 10.1007/s10584-012-0432-6.
792 Salado, J. and G. Marjolet (1975), Contribution à l'étude de l'aquifère karstique de la
793 source du Lez (Hérault). II. Etude du chimisme des eaux de la source du Lez et de son bassin.
794 Université Montpellier 2. Mémoires du C.E.R.G.A, Tome IX-Fac. II. 101p.
795 Salerno, F., and G. Tartari (2009), A coupled approach of surface hydrological
796 modelling and Wavelet Analysis for understanding the baseflow components of river
797 discharge in karst environments. J. Hydrol., 376: 295–306.
798 Schaefli, B., D. Maraun, and M. Holschneider (2007), What drives high flow events in
799 the Swiss Alps? Recent developments in wavelet spectral analysis and their application to
800 hydrology. Advances in Water Resources 30: 2511–2525.
801 Slimani S, Massei N, Mesquita J, Valdés D, Fournier M, Laignel B, Dupont JP. 2009
802 Combined climatic and geological forcings on the spatio-temporal variability of piezometric
803 levels in the chalk aquifer of Upper Normandy (France) at pluridecennal scale. Hydrogeology
804 Journal 17: 1823–1832

Thiery, D., P. Bérard, and A. Camus (1983), Captage de la source du Lez. Etude de relation entre la source et son réservoir aquifère – rapport n°1 : recueil des données et établissement d'un modèle de cohérence. Rapport BRGM 83SGN 167 LRO

Thiery, D., and P. Bérard (1984), Alimentation en eau de la Ville de Montpellier - Captage de la source du Lez. Etude des relations entre la source et son réservoir aquifère – rapport n°3 : modèle d'étude détaillé. Rapport BRGM 84-AGI-171-LRO/EAU

Torrence, C., and G.P. Compo (1998), A practical guide to wavelet analysis. Bull. Am. Met. Soc. 79, 61–78.

Torrence, C., and P.J. Webster (1999), The annual cycle of persistence in the El Niño/ Southern Oscillation. Quart. J. R. Met. Soc. 124: 1985–2004.

816 Table 1: Guide to hydrological variables providing keys to interpret the response of the
817 hydrological system to stressors; relationships underlined in grey are used in the present
818 study.

819

Stressors		**Karst response**		
	Input variable used to characterize stressors		**Output variable used to characterize the karst response**	
			Qr	***h* or *s***
			Residual discharge	**Groundwater level or drawdown**
Climatic pressure	***P***	*Input-Output relationships*	***P-Qr***	***P–h* or *P-s***
	Precipitation	*Highlight:*	Hydrogeological response	*Relationship disrupted by pumping*
Anthropic pressure	***Qp***	*Input-Output relationships*	***Qp-Qr***	***Qp-s***
	Pumping discharge	*Highlight:*	*Relationship disrupted by precipitation*	Storage mobilization
Climatic and anthropic pressures	***Qs***	*Input-Output relationships*	***Qs-Qr***	***Qs-s***
	Karst storage flow mobilized by pumping	*Highlight:*	Groundwater stress due to active water management during low groundwater level periods	Level of stress on the groundwater resource

820

821

822 Figure 1: Hydrogeological map of the Lez karst system.

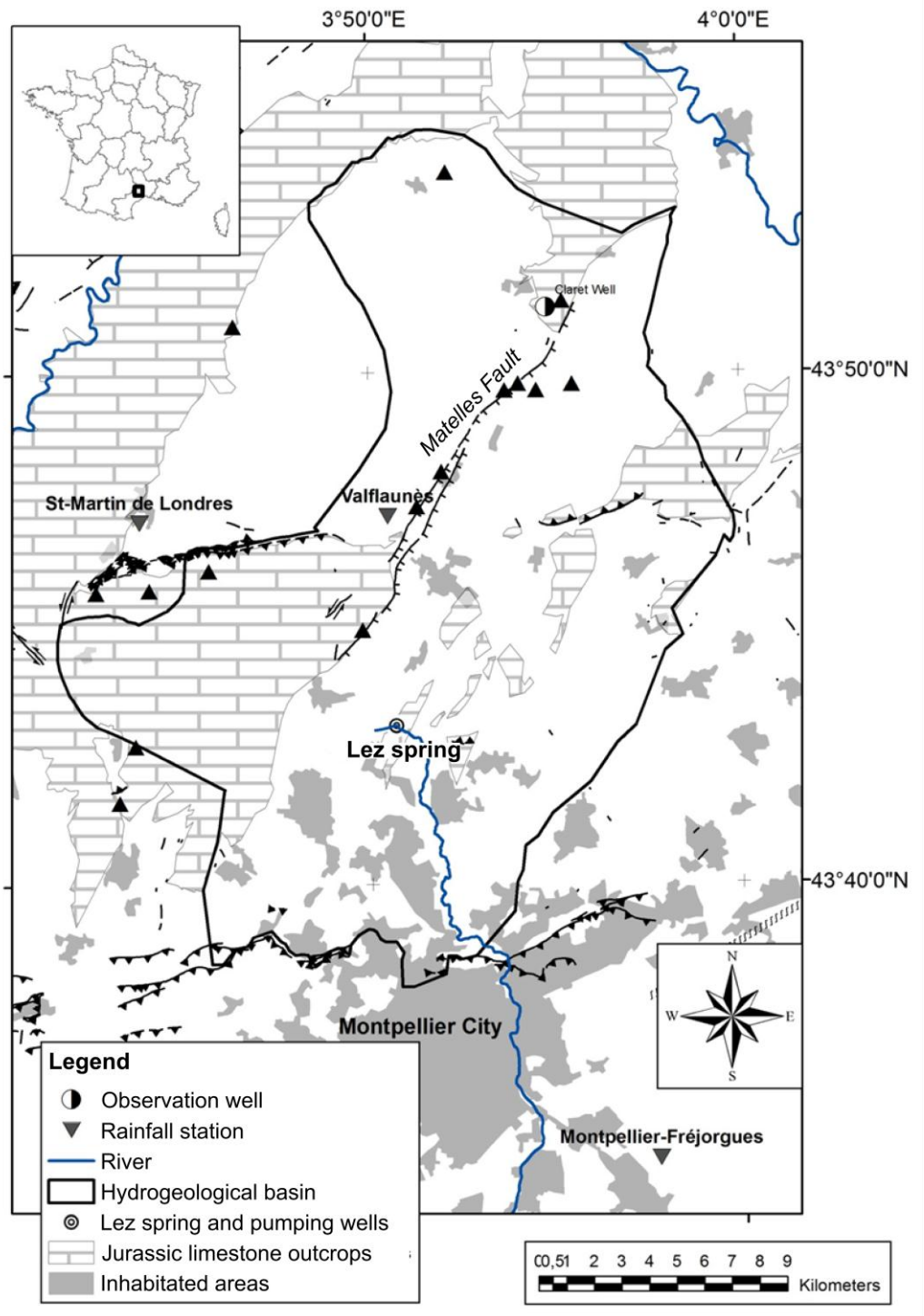

823

824

825 Figure 2: Cross section of the karst network at the outlet of the Lez aquifer, showing the
826 location of the spring and of the pumping station; Piezometric levels are also plotted
827 according to high (2a) and low (2b) flow conditions.

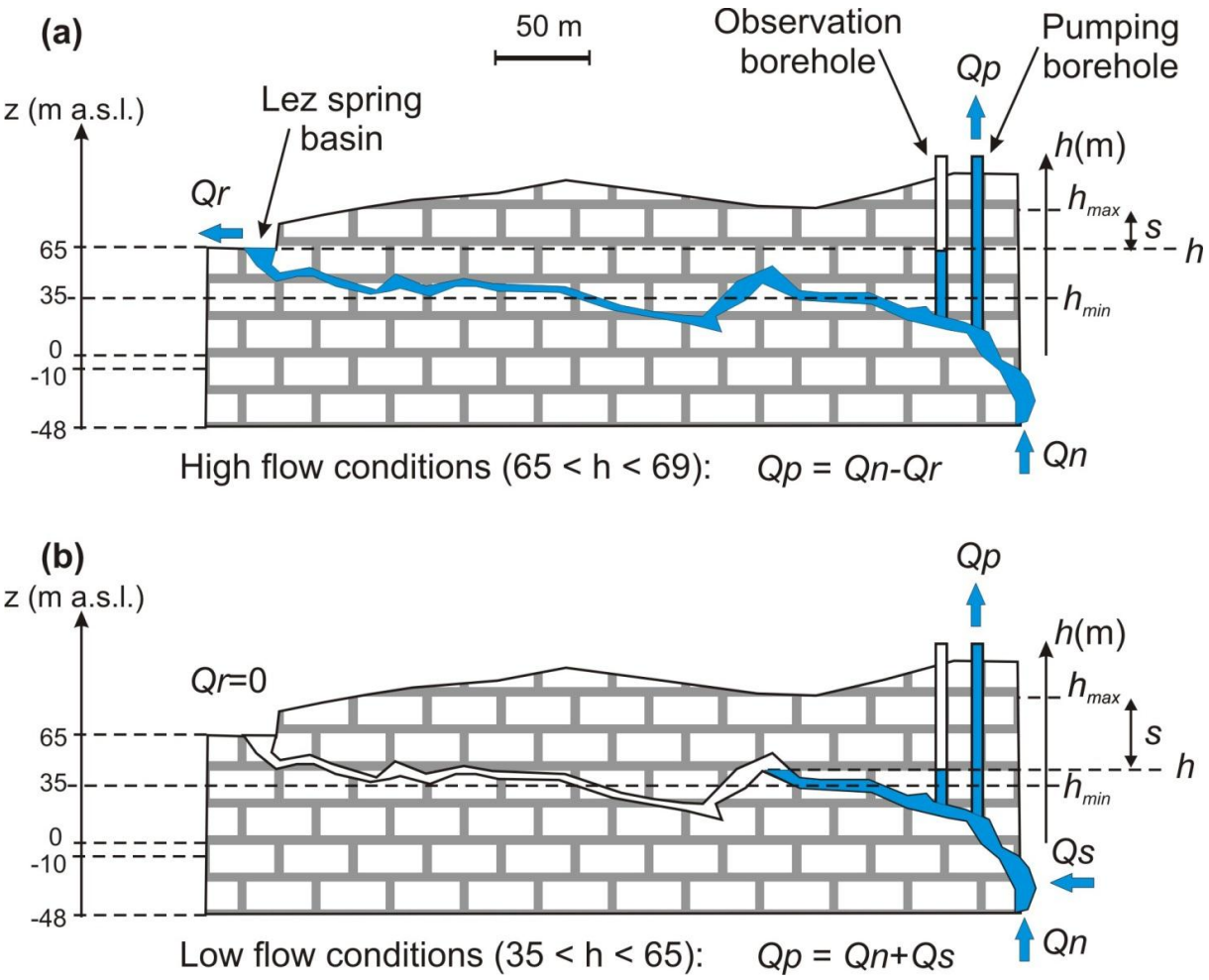

828

829

Figure 3: Hydrogeological daily time series of the Lez karst system from 01 June 1974 to 31 December 2011 (a), and a zoom on the 2002-2003 hydrological cycle (b); from top to bottom: precipitation (*P*), measured pumping discharge (*Qp*) and calculated storage discharge mobilized by pumping (*Qs*), measured Lez residual discharge (*Qr*) and simulated natural discharge (*Qn*), and the measured groundwater level in the conduit (*h*).

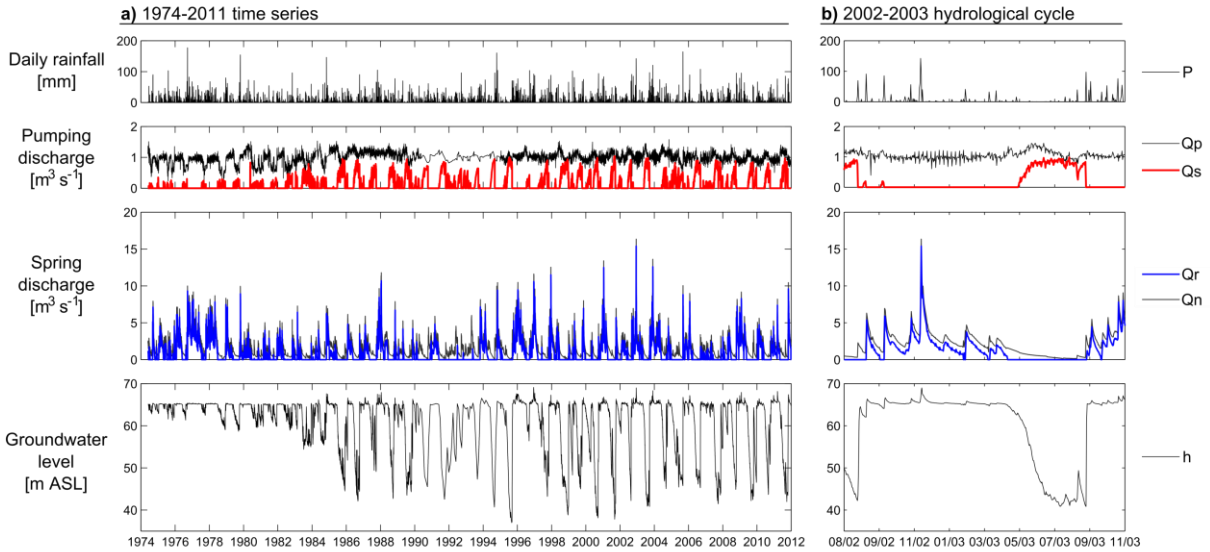

Figure 4: Annual evolution of hydrogeological time series expressed as deviation from the mean; the annual hydrological cycle was delimited from August to July.

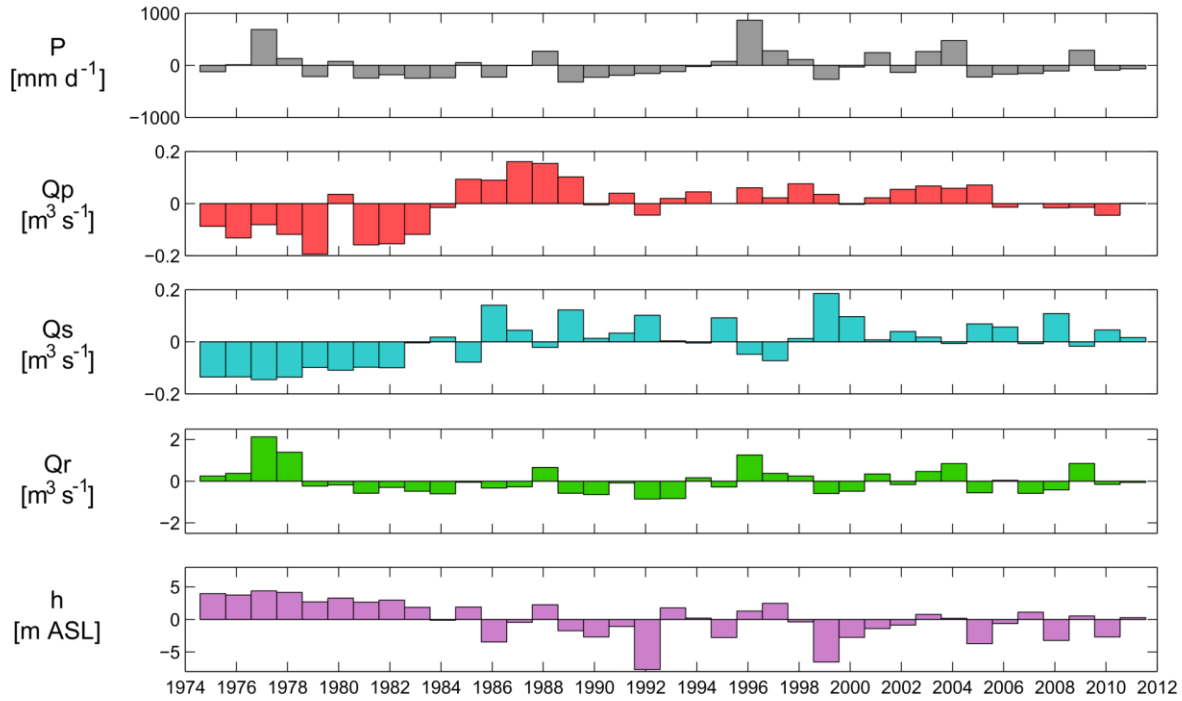

Figure 5: Multiresolution analysis of daily hydrogeological time series using Daubechies 20 wavelets; different components of the decomposition correspond from top to bottom to short-scale to long-time scale processes, with level *j* corresponding to time scales at 2^{j-1}; grey rectangles indicate a lack of data for the first levels 1 to 3 (1 to 4-day resolution) during a period of weekly raw data.

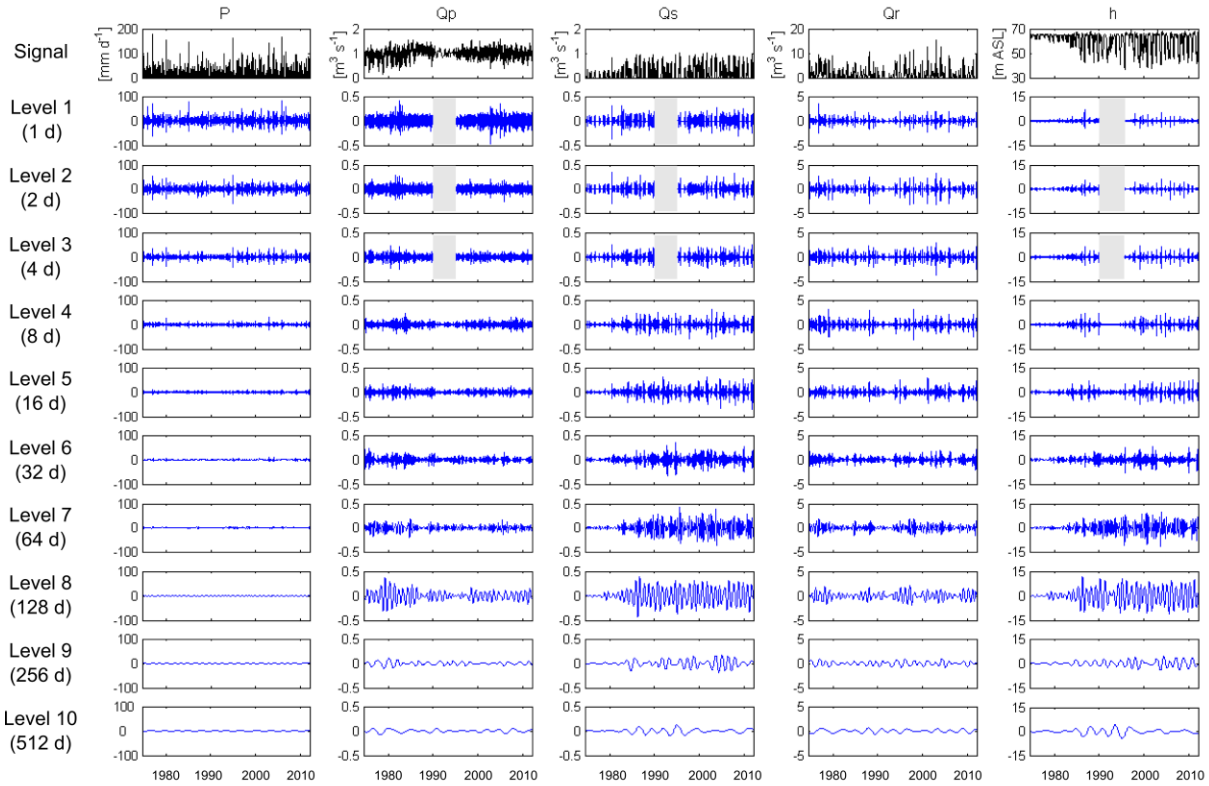

848 Figure 6: Standard deviation by multiresolution levels (from level 1 to level 14) of the
849 standardized hydrogeological signals.

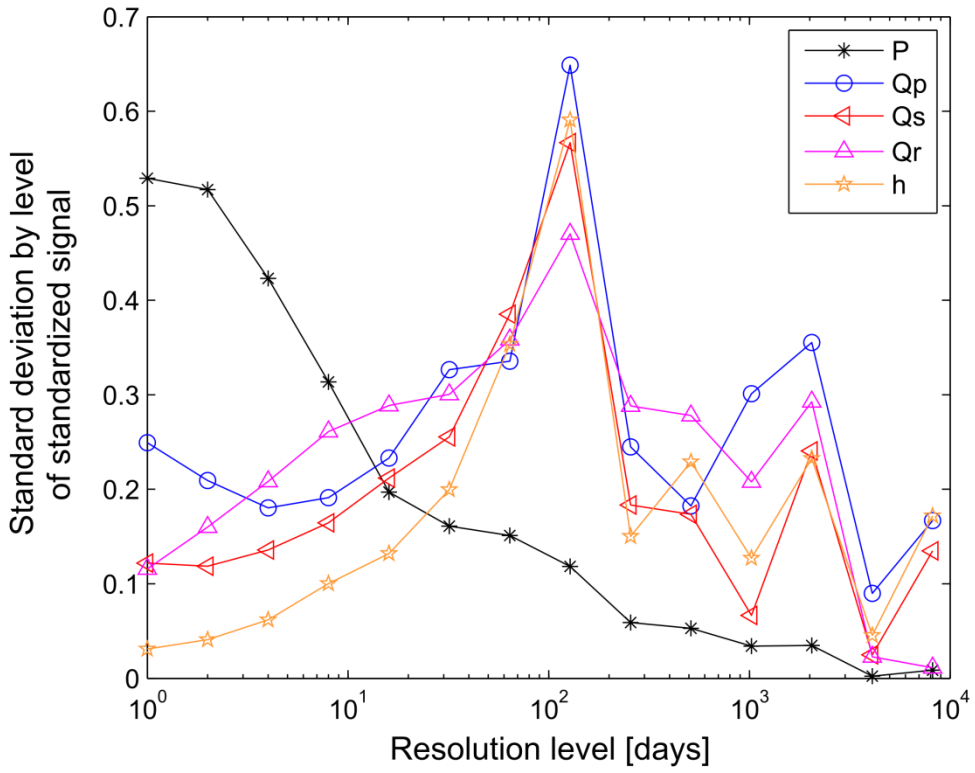

850

851

Figure 7: Cross-correlation functions (CCF) applied at different scales of the multiresolution analysis with: *P*-*Qr* CCF (7a), *Qp*-*s* CCF (7b), *Qs*-*Qr* CCF (7c), and *Qs*-*s* (7d); two cases are shown for each plot: i) CCF between two signals at the same multiresolution level *j* (black circles), and ii) CCF between an overall input signal (i.e. a non-decomposed time series) and an isolated output signal at a given multiresolution level *j* (green stars). Maximum CCF values (*Rmax*) are expressed as a function of the multiresolution levels in days (at level *j*, the resolution corresponds to 2^{j-1} days). *Rmax* values are also plotted for CCF between two overall signals (dashed blue line).

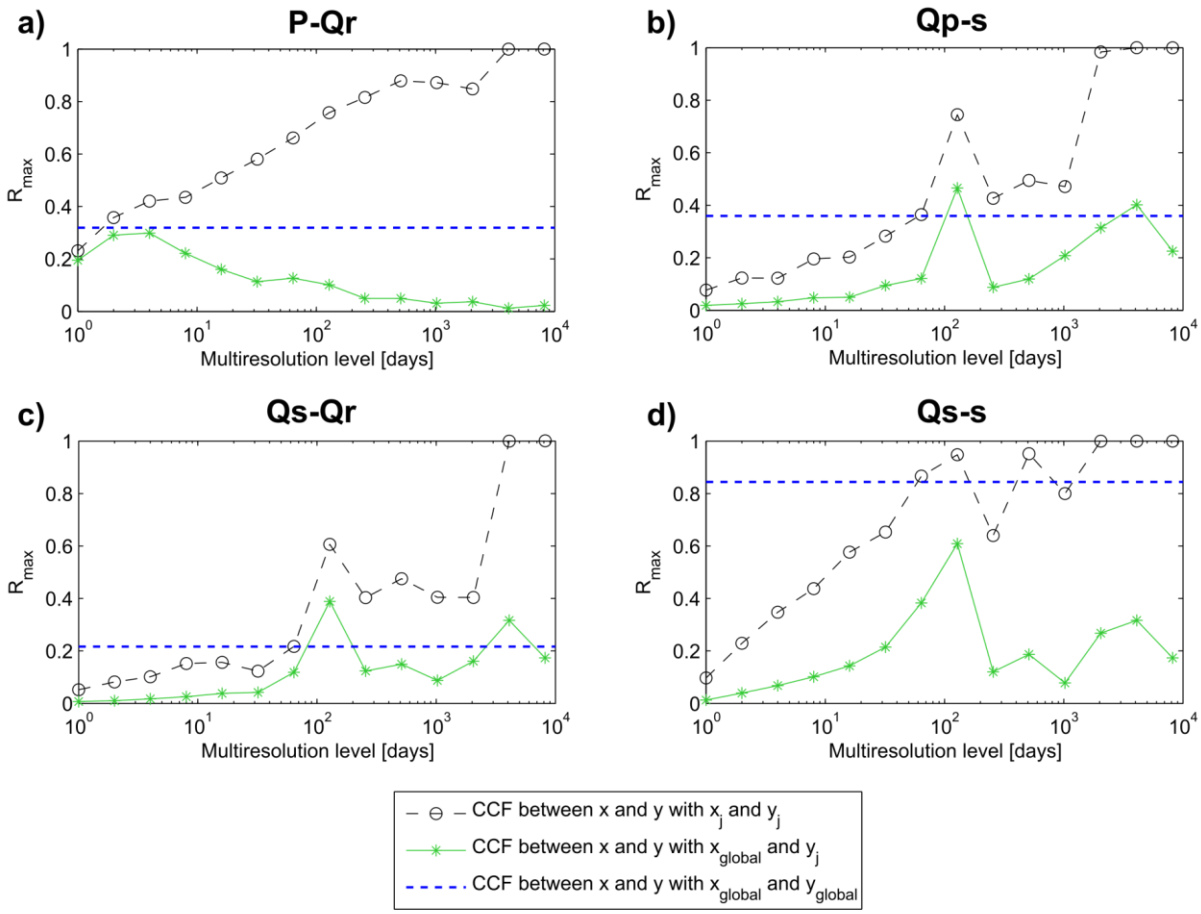

Figure 8: Continuous wavelet power spectra of the hydrogeological time series; the thick black outline designates the 5% significance level against red noise and the cone of influence, where edge effects might distort the picture, is shown in a lighter shade.

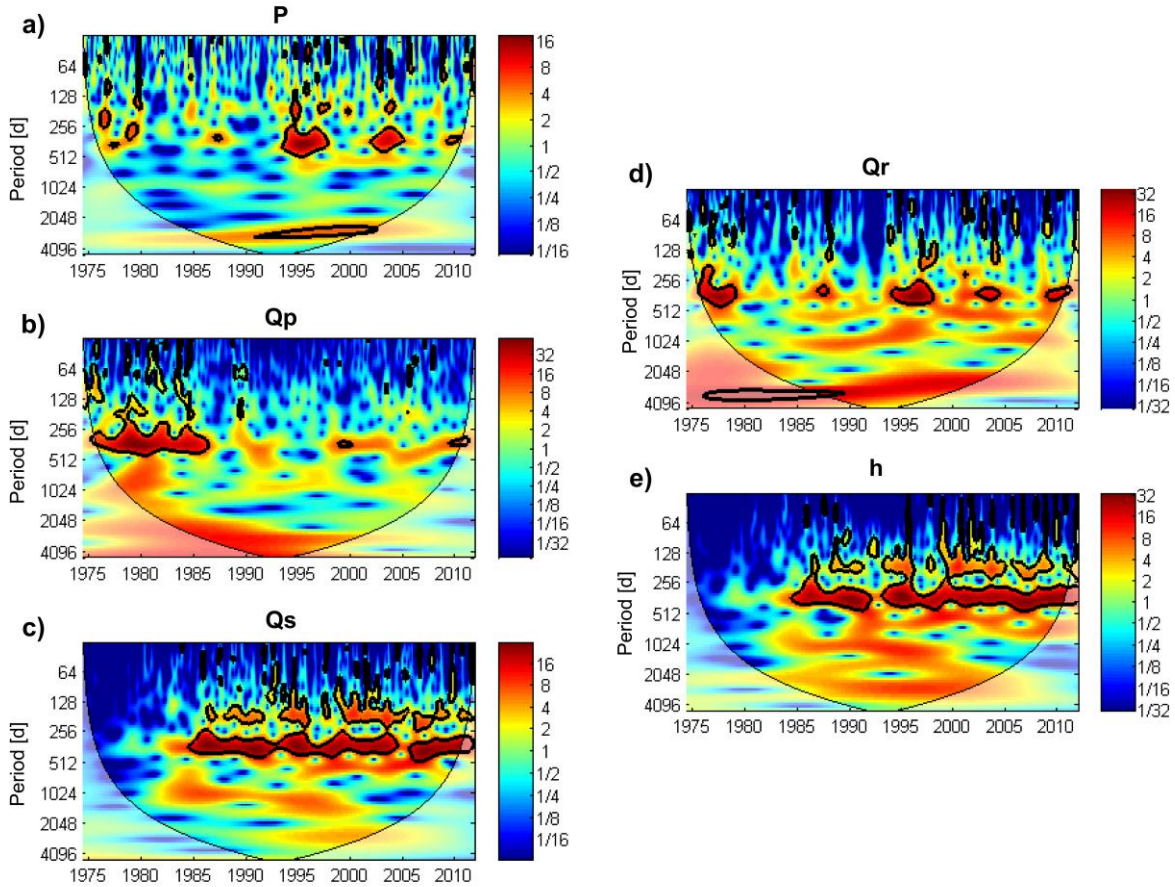

867 Figure 9: Cross wavelet (XWT) and wavelet coherence (WTC) spectra between (9a and 9b)
868 rainfall and residual Lez discharge *P-Qr*, (9c and 9d) pumping and drawdown *Qp-s*, (9e and
869 9f) groundwater stress and residual Lez discharge *Qs-Qr*, and (9g and 9h) groundwater stress
870 and drawdown *Qs-s*; The thick black outline designates the 5% significance level against red
871 noise and the cone of influence where edge effects might distort the picture is shown as a
872 lighter shade.

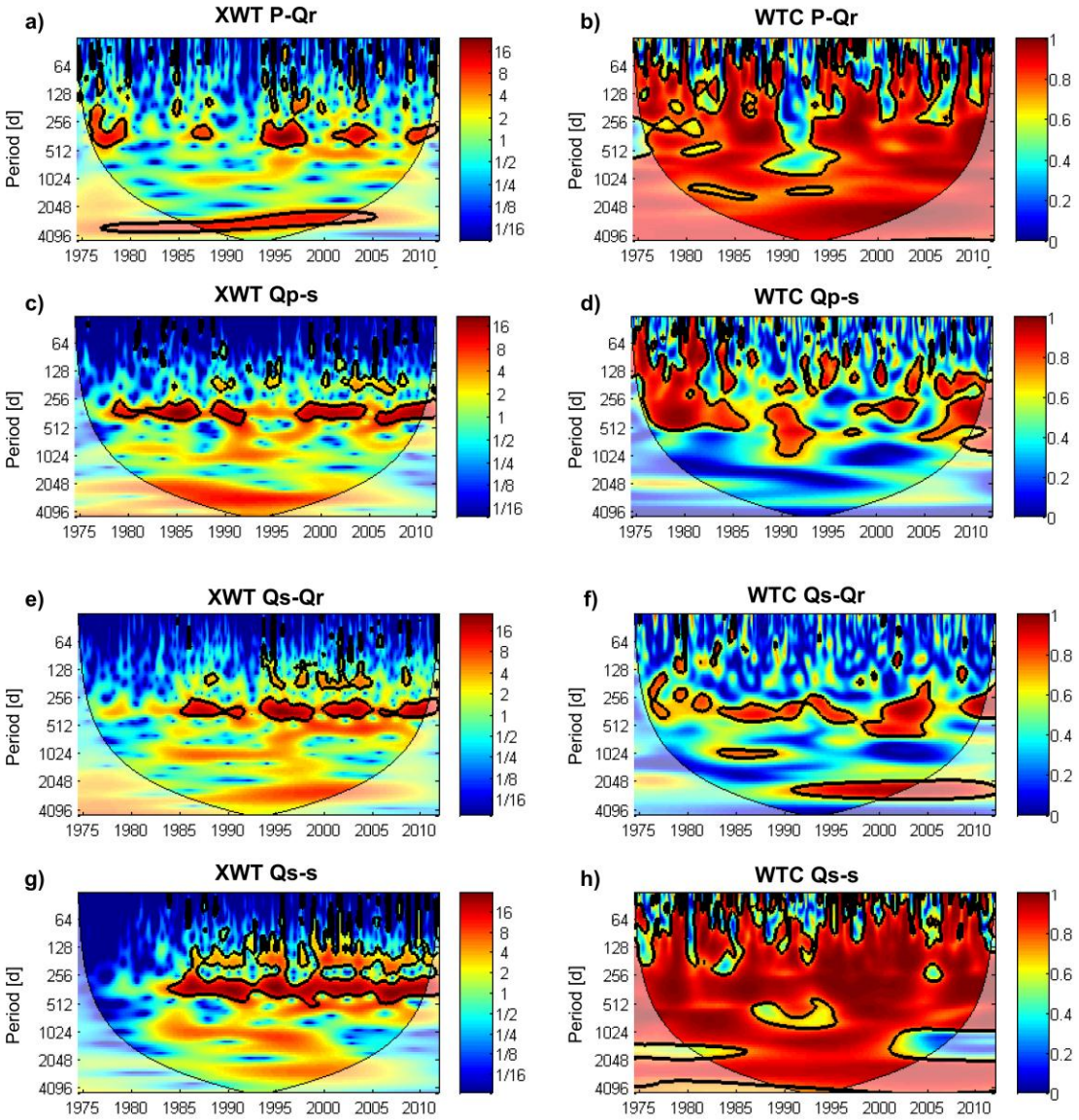

873